European Review for Medical and Pharmacological Sciences 2023; 27: 5039-5052

Effect evaluation of denosumab combined with curettage and bone cement reconstruction in the treatment of recurrent giant cell tumor of bone around the knee joint

D.-K. DUAN[1,2], G.-C. ZHANG[1], B.-J. SUN[2], T.-X. MA[1], M. ZHAO[1]

[1]Department of Musculoskeletal Tumor, The Third Hospital of Hebei Medical University, Shijiazhuang, China
[2]Department of Musculoskeletal Tumor, The First Hospital of Handan, Handan, China

Abstract. – OBJECTIVE: Giant cell tumor of bone (GCTB) is a common primary bone tumor with latent malignant tendency. GCTB is prone to occur around the knee joint, and surgery is the major treatment method. There are relatively few reports on denosumab in the treatment of recurrent GCTB around the knee joint and postoperative function evaluation of patients. This research aimed to explore the appropriate surgical options for the treatment of recurrent GCTB around the knee joint.

PATIENTS AND METHODS: 19 patients with recurrent GCTB around the knee joint, who were admitted to Hospital for 3 months following denosumab treatment from January 2016 to December 2019, were included as the research subjects. The prognosis was compared between patients treated with curettage combined with polymethylmethacrylate (PMMA) and those with extensive-resection replacement of tumor prosthesis (RTP). A deep learning model of Inception-v3 combined with a Faster region-based convolutional neural network (Faster-RCNN) was constructed to classify and identify X-ray images of patients. The Musculoskeletal Tumor Society (MSTS) score, short form-36 (SF-36) score, recurrence, and the rate of complications were also analyzed during the follow-up period.

RESULTS: The results showed that the Inception-v3 model trained on the low-rank sparse loss function was obviously the best for X-ray image classification, and the classification and identification effect of the Faster-RCNN model was significantly better than that of the convolutional neural network (CNN), U-Net, and Fast region-based convolutional neural network (Fast-RCNN) models. During the follow-up period, the MSTS score in the PMMA group was significantly higher than that in the RTP group ($p<0.05$), while there was no significant difference in the SF-36 score, recurrence, and the rate of complications ($p>0.05$).

CONCLUSIONS: The deep learning model could improve the classification and identification of the lesion location in the X-ray images of GCTB patients. Denosumab was an effective adjuvant for recurrent GCTB, and widely extensive-resection RTP could reduce the risk of local recurrence after denosumab treatment for recurrent GCTB.

Key Words:
Knee joint, Recurrent giant cell tumor of bone, Polymethylmethacrylate, Replacement of tumor prosthesis, Deep learning.

Introduction

Giant cell tumor of bone (GCTB) is a very common and active-growth primary bone tumor which causes strong bone erosion. It mostly occurs around the knee joint, distal radius, sacrum, and spine. The morbidity is the highest especially around the knee joint[1]. The treatment of GCTB mainly depends on the surgery. The most commonly used surgical methods include curettage and bone transplantation, polymethylmethacrylate (PMMA) bone cement, and tumor segment resection with artificial prosthesis replacement, but the postoperative recurrence can reach 40-60%[2]. Since the knee joints are one of the main weight-bearing joints of the lower limbs, with a large amount of activity and complex joint functions, artificial prostheses and large bone block transplantation cannot meet the needs of the strong support structure of the knee joints. Therefore, the combination of GCTB curettage with PMMA bone cement has become a standard treat-

Corresponding Author: Guo-Chuan Zhang, MD; e-mail: hbsygzlhy@163.com

ment option for GCTB[3]. However, some scholars[4] have pointed out that the PMMA bone cement under the articular surface will cause damage to the articular cartilage, leading to iatrogenic osteoarthritis and adverse effects on joint function.

With modern physical and chemical adjuvant therapies, and continuous advancement in early diagnosis and surgical reconstruction of bone tumors, the recurrence after GCTB treatment can be reduced to 10-20%, and the limb salvage rate has gradually increased[5]. Lesion resection can be used in the treatment of local recurrence in patients with limb GCTB, but surgical resection alone would lead to serious complications[6]. Surgery performed under the protection of denosumab can improve the prognosis of patients and reduce the recurrence rate[7]. Some studies[8] have confirmed that preoperative use of denosumab in patients with GCTB can thicken the cortex of bone and subchondral bone in patients and make the boundary of tumors clear. Denosumab can also lower the number of surgeries performed in individual GCTB patients, thereby preserving joints and improving postoperative joint function[9]. However, wide attention has been drawn to whether the increase in intralesional septation and sclerosis caused by denosumab administration affects the difficulty of curettage surgery.

It is of great significance to monitor the recurrence with X-ray and other imaging methods for improving the function and stability of the knee joints in patients with GCTB after surgery[10]. X-ray has the advantages of high definition and high contrast for bone tissue imaging. To extract useful information from a large amount of imaging data, artificial intelligence technologies such as machine learning and deep learning have been widely applied in the mining of medical imaging data[11]. Deep learning has achieved breakthroughs in target recognition, language recognition, computer vision, and other fields. Deep learning algorithms can also get excellent results in the classification and identification of X-ray images[12].

To this end, a deep-learning model was constructed for GBTB image classification and identification. The effect of curettage combined with PMMA and extensive-resection replacement of tumor prosthesis (RTP) was also analyzed after denosumab was given for the treatment of recurrent GCTB around the knee joints. We hope this work can provide a reference for improving the prognosis and finding a safe and reliable treatment method for patients with recurrent GCTB around knee joints.

Patients and Methods

Research Objects and Grouping

106 GCTB patients who were treated in the center from January 2016 to December 2019 were selected as the research subjects. Inclusion criteria: (1) GCTB located around the knee joint. (2) Patients who were diagnosed with GCTB by clinical signs, imaging examinations, and histopathological examinations. (3) Patients treated with limb salvage surgery. (4) Patients with a postoperative follow-up of more than 12 months. Exclusion criteria: (1) Patients who had not complete clinical data. (2) Patients who were lost or died during the follow-up period. (3) Patients with complicated diseases such as those concerning the hematological system, malignant tumors, and infections. According to the above criteria, 79 GCTB patients were retrieved, of which 3 cases were lost to follow-up, 1 case was amputated for malignant transformation, 1 case was treated with knee arthrodesis, 1 had the GCTB in the fibular head, and 1 got the lesion in the patella. Apart from those above, 50 cases were without recurrence, and 3 took no denosumab. A total of 19 patients were included in this research at last. The process of inclusion and exclusion of patients is shown in Figure 1. This study has been approved by the Ethics Committee of the First Hospital of Handan (approval number: 2023-L-005).

All 19 patients were treated with six doses of denosumab for 3 months before surgery, having subcutaneous injections on days 1, 8, 15, and 29, followed by 120 mg in the first month. The patients were divided into two groups according to their surgical methods. PMMA group (n=12) consisted of 5 cases with GCTB in the distal femur and 7 cases in the proximal tibia. RTP group (n=7) was made up of 3 cases with GCTB in the distal femur and 4 cases in the tibia. All the patients received special RTP with extensive resection.

Data Collection

The general information of the patients was collected before surgery, including their age, gender, tumor location, and Campanacci imaging grade. The data collected after surgery included recurrence, follow-up time, Musculoskeletal Tumor Society (MSTS) score, and short form-36 (SF-36) score. The Campanacci imaging grading was as follows: grade I (resting lesions) was usually in the cancellous bone, with a clear boundary and a thin sclerosis zone. For the grade II (active lesions), thinning and swelling of the cortical bone could be observed, the boundary was clear, the

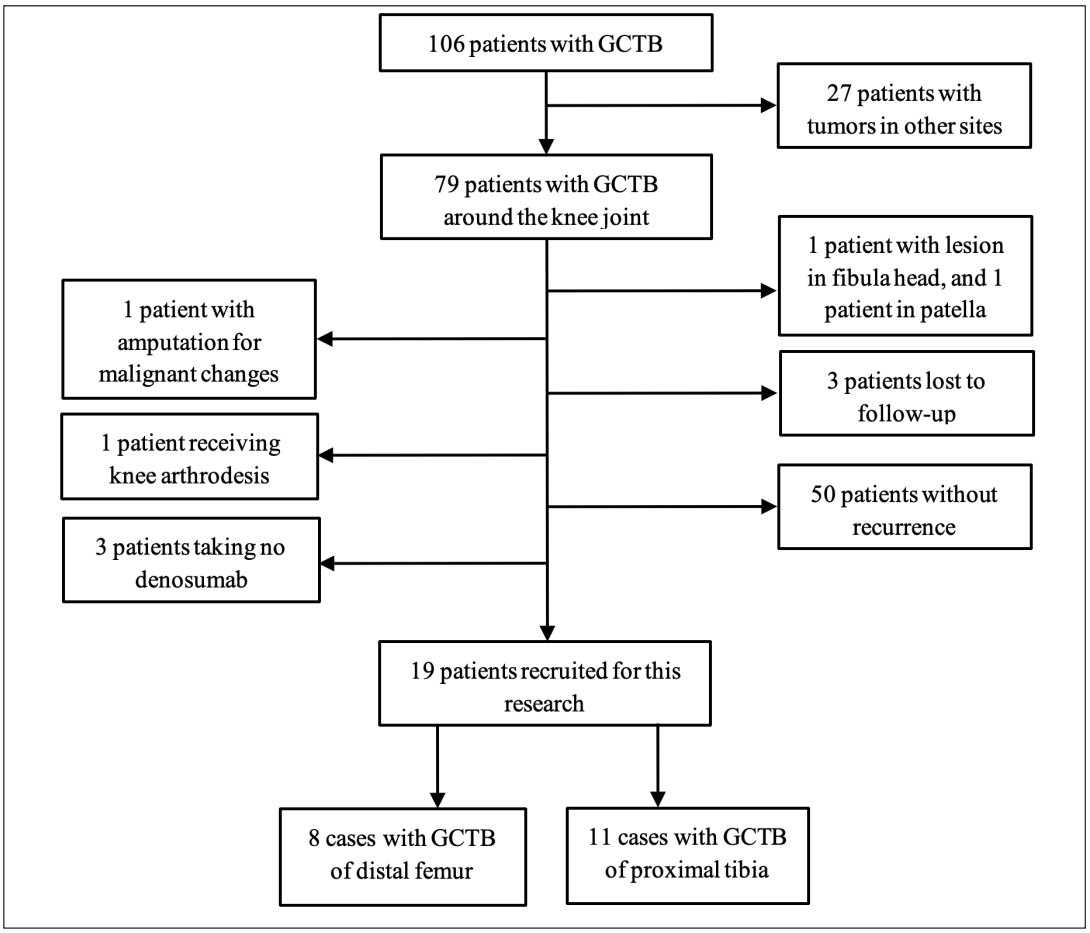

Figure 1. Flow chart of inclusion and exclusion for patients included in this research.

sclerosis zone was absent, and the morphology of an aneurysmal bone cyst was shown. For the grade III (invasive lesions), the lesions penetrated the cortical bone and entered the soft tissue, and there was no periosteal encapsulation. MSTS score was composed of 6 items, the full score of each item was 5, and the total score was 30. The higher the MSTS score, the better the lower limb function of the patient. For the SF-36 score, the full score of each item was 100; the higher the SF-36 score, the better the quality of life of the patient. X-ray, computerized tomography, magnetic resonance imaging, and other imaging techniques were applied to evaluate the recurrence of local GCTB in patients.

Surgical Methods for Different Groups

After general anesthesia and nerve block anesthesia, the patient was placed in a supine position. The tourniquet was taken to wrap around the affected leg and thigh, and the surgery was performed under a pressure of 50-60 kPa to reduce bleeding.

In the RTP group, a longitudinal incision was made in the femoral end, from 5 cm of the upper edge of the femoral lesion to the plane of the knee joint. The cambered incision of the tibial end was at the upper lateral side of the tibia, as the upper end of the knee joint was 1 cm from the lateral clearance, forward arc to the outer edge of the tibial crest, and the lower end was 5 cm below the lower edge of the tibial lesion. In the PMMA group, the original incision in the skin, muscle, and bone were removed in fusiform shape. The internal fixation device, bone cement, or bone filling that had been retained in the previous surgery were removed, and the field of view was further enlarged. The lesions were scraped one layer by one layer along the inner wall of the tumor. The inner wall of the lesions was polished with a high-speed grinding drill to remove the sclerosing edge, and the pulse flushing gun was repeatedly rinsed. The inner wall of the tumor shell was cauterized with an argon knife and soaked with distilled water for 5 min.

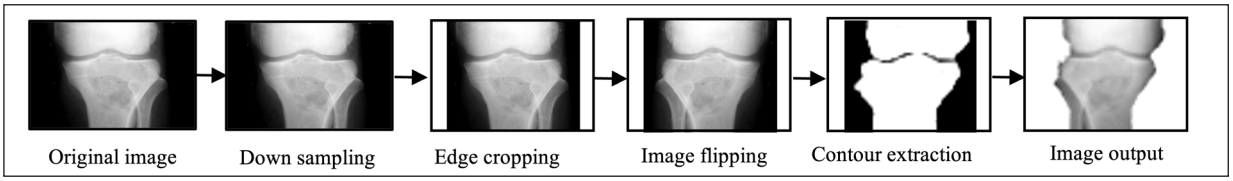

Figure 2. Pre-processing of an image of patients

The lesion was rinsed again, the cavity was filled with PMMA, and internal fixation was used if necessary. The drainage tube was indwelled after surgery, and the drainage volume was less than 30 mL. 2 weeks after the surgery, functional exercise was conducted gradually. Weight-bearing on the affected limb should be avoided for 3 months.

In the RTP group, the osteotomy plane was determined according to the preoperative imaging data, and the tumor was extensively resected 5 cm outside the tumor response zone. The pulse rinse gun was used for repeated washing, and a special tumor prosthesis was installed. The proximal tibia prosthesis was covered with medial gastrocnemius muscle flap, to reconstruct the patellar ligament insertion. The drainage tube was also indwelled after surgery, with a drainage volume of less than 30 mL. 4 weeks after the soft tissue was healed, flexion and extension movement of the joint was started to train walking.

Image Preprocessing

Image preprocessing is one of the essential links in image understanding and analysis. Preprocessing can eliminate irrelevant information in the original image and enhance useful information related to the target; therefore, good image preprocessing can improve the performance of the algorithm[13]. Image preprocessing was carried out to eliminate the differences in imaging quality among individuals, and the processing method is shown in Figure 2.

Downsampling

The X-ray images of patients had the characteristics of high resolution and high definition, which was helpful for doctors to observe the texture and other features of the lesion location. However, the high-resolution X-ray image would affect the processing efficiency. Thus, the down-sampling was utilized to crop the original image in units of 5 pixels, so as to obtain the down-sampled image.

Cropping of image edges

There were interference or noise bands of different pixel units around the image, which greatly affected the processing effect of the algorithm. Thus, the edge strips in the down-sampled image were cropped, to obtain the edge-cropped image.

Image flipping

Because the bone structure of the human body is symmetrically distributed, radiologists often collect image data of the contralateral bone structure to obtain left and right bone X-ray images. In this research, the acquired bone X-ray images were flipped to obtain X-ray images with the same orientation.

Extraction of bone contours

The background regions of the bone X-ray images were marked, and then the redundant background was eliminated. The original image was converted into a binary image using the Otsu method, then the processed image was morphologically filtered. The boundary of the bone structure was obtained after the connected regions were marked, and the preprocessed image was obtained by cutting the background region.

Image Classification Under Deep Learning Model

The Inception-v3 network model was applied for the classification of preprocessed X-ray images. The basic structure of the Inception-v3 network model is displayed in Figure 3.

When the Inception-v3 network model was applied to extract the features in the X-ray images, the input image was first defined as I, and the feature map was F after multi-channel processing using the convolutional layer and the pooling layer. A linear logistic regression function with shared weights was added after the convolutional layer, and the sigmoid function was adopted in the output layer. Therefore, the probability of obtaining the lesion location (x, y) from the feature map F was expressed in Equation (1).

$$p_{x,y}=\text{Sigmoid}\,(\sigma\cdot F_{x,y}+b) \quad (1)$$

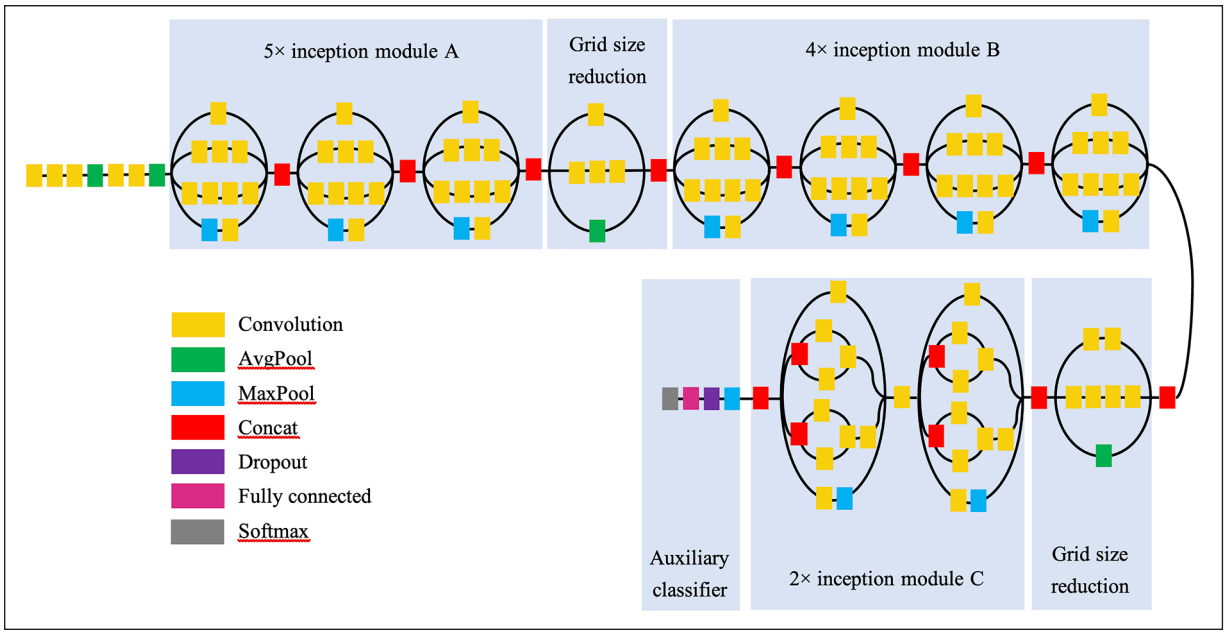

Figure 3. The basic structure of the Inception-v3 network model.

In Equation (1), was the weight value in logistic regression, and b was the bias.

In the process of training the Inception-v3 network model, different loss functions were used to train model parameters, in which different processing effects were obtained. The effects of binary cross-entropy logistic regression (LR) loss function, max pooling (MP) loss function, label assignment (LA) loss function, sparse assign (SA) loss function, and low rank sparse (LRS) loss function were compared and analyzed on the classification performance of Inception-v3 network model.

LR loss function

The standard formulation of the LR loss function was expressed in Equation (2).

(2)

$$LR(Y,P(Y|X))=-\log P(Y|X)$$

(3)

$$y|x) = \begin{cases} \frac{1}{1+e^{-f(x)}} \\ \frac{1}{1+e^{f(x)}} \end{cases}$$

in Equation (3) was substituted into Equation (2) of LR, then the objective function was regularized. Finally, a new objective function as Equation (4) was obtained.

(4)

$$Aim(\Theta) = -\frac{1}{m}\sum_{i=1}^{m}[y_i \log h_\Theta(x_i) + (1-y_i)\log(1-h_\Theta(x_i))] + \frac{\lambda}{2m}\sum_{j=1}^{n}\Theta_j^2$$

MP loss function

It was assumed that the probability of lesions in the target region was close to 1, then the probability of lesions in the overall image I could be expressed as Equation (5).

(5)

$$P(y=1|I,\mu)=\max\{p_1,p_2,\cdots,p_m\}$$

(6)

$$Loss = -\sum_{n=1}^{N} Exp_{y_n} \log[p(y_n|I_n,\mu)] + \frac{\lambda}{2}\|\mu\|^2$$

In Equation (5) and Equation (6), N was the total number of images, was the image label, λ was the control regular term for model complexity, was the empirical estimate of , and μ was the depth parameter of the network.

LA loss function

It was assumed that the labels in the image I were consistent with the predicted labels, and the rest of the labels were negative. Thereby, the weighted cross-entropy loss function was expressed in Equation (7).

(7)

$$\text{Loss} = -\sum_{n=1}^{N}\left(\sum_{j=1}^{k}\text{Exp}'\log\left(P(y=1|P_j',\mu)\right) + \sum_{j=k+1}^{k}\text{Exp}'\log\left(P(y=0|P_j',\mu)\right)\right) + \frac{\lambda}{2}\|\mu\|^2$$

SA loss function

The coefficient restriction term was added to the MP loss function, so the SA loss function could be expressed as Equation (8).

(8)

$$\text{Loss} = \sum_{n=1}^{N}\left(-\text{Exp}_{y_n}\log\left(p(y_n|I_n,\mu)\right) + \eta\|p'_n\|_1 + \varepsilon\|P_n\|_2\right) + \frac{\lambda}{2}\|\mu\|^2$$

In Equation (8), was the norm of Loss, and was the sparse factor.

LRS loss function

The positive samples in the X-ray data set were sparse, and concentrated in the bone structure region. The mathematical expression of the LRS loss function could be written as Equation (9).

(9)

$$\text{Loss} = \sum_{n=1}^{N}\left(-\text{Exp}_{y_n}\log\left(p(y_n|I_n,\mu)\right) + \eta\|p'_n\|_1 + \varepsilon\|P_n\|_2\right) + \frac{\lambda}{2}\|\mu\|^2$$

In Equation (9), was the kernel norm of the matrix , and was the low-rank constraint factor.

The receiver operator characteristic (ROC) curves were drawn under different loss functions. In this research, the accuracy and the area under the ROC curve (AUC) were selected for the evaluation of the classification performance. The accuracy was calculated through Equation (10).

(10)

$$\text{Accuracy} = \frac{TP+TN}{TP+TN+FP+FN}$$

In Equation (10), TP represented the number of true positive samples, TN represented the number of true negative samples, FP was the number of false positive samples, and FN was the number of false negative samples.

When drawing a ROC curve, the horizontal and vertical axes represented the false positive rate (FPR) and the true positive rate (TPR), respectively. Thus, the AUC was described as Equation (11), and the FPR and TPR were expressed as Equation (12).

(11)

$$AUC = \int_0^1 ROC dr$$

(12)

$$\begin{cases} TPR = TP/(TP+FP) \\ FPR = FP/(FP+TN) \end{cases}$$

Target Region Detection under Deep Learning Model

With the Faster-RCNN model, the target regions in X-ray images were detected. The basic steps of the Faster-RCNN model for target detection were as follows: (1) the image to be detected was input into the convolutional neural network (CNN) model. (2) The proposed region was generated through the region proposal network, and an appropriate amount of proposal windows were reserved. (3) The proposal windows were mapped to the feature map of the last convolutional layer of CNN, and the region of interest (ROI) pooling operation was utilized to obtain feature maps of different sizes. (4) The Softmax classifier was applied for image classification, and the linear regression model was adopted for edge prediction (Figure 4).

The region proposal network and the Fast-RCNN model were adopted alternately for the training of the Faster-RCNN model. The mathematical expressions of the loss functions in the region proposal network and Fast-RCNN model were Equation (13) and Equation (14), respectively.

(13)

$$\text{Loss}_1 = \frac{1}{N_c}\sum_i L_c(p_i, p_i^*) + \alpha\frac{1}{N_r}\sum_i p_i^* L_r(q_i, q_i^*)$$

(14)

$$\text{Loss}_2 = L_c(p,u) + \alpha[u \geq 1]L_l(q^u, v)$$

In Equation (13) and Equation (14), i represented the index of the selected box, was the judged log loss of the subject, was the regression loss, was the number of checked boxes, and was the number of positions of checked boxes. was the predicted probability of the index i belonging to a certain category, was the coordinate of the predicted frame, and α was the loss balance constant of 10.

Afterward, indicators of the recall rate, the classification precision, and the mean average precision (MAP) were chosen to evaluate the performance of target region segmentation.

Statistical Analysis

SPSS 19.0 statistical software (IBM Corp., Armonk, NY, USA) was applied for statistical processing and analysis of the result data. Measurement data were expressed as mean±standard deviation , and statistical analysis was performed using the least significant difference *t*-test. Enu-

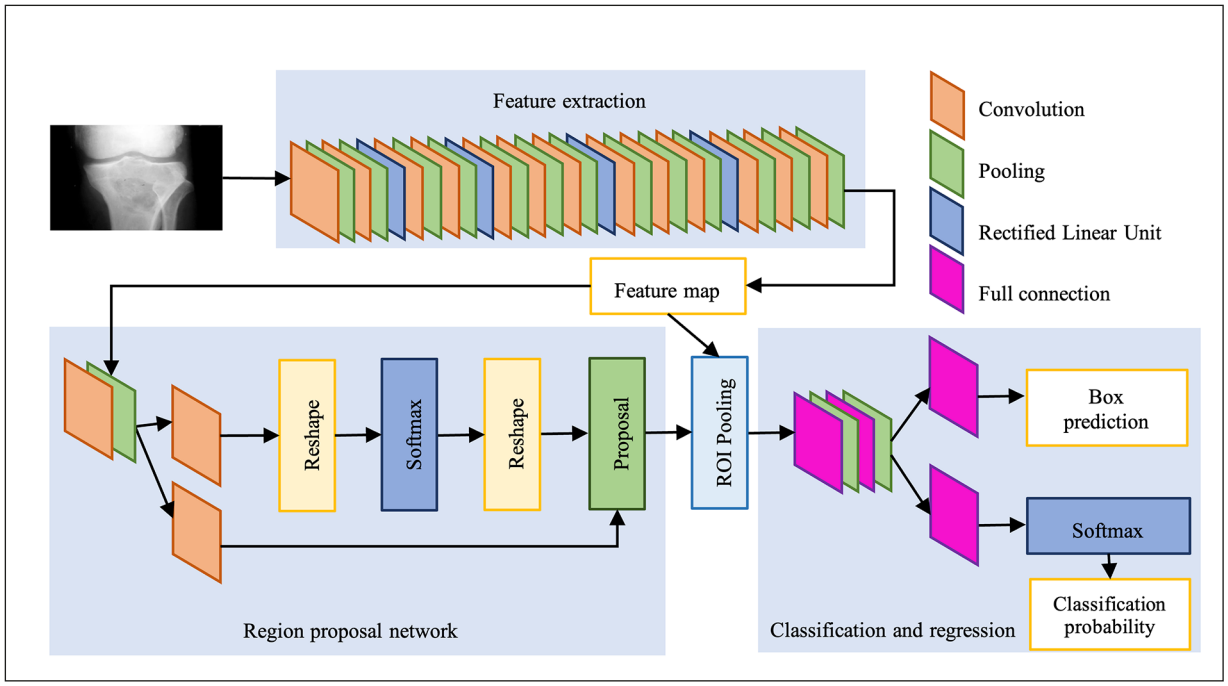

Figure 4. The basic structure of the Faster-RCNN model.

meration data were expressed by frequency (percentage), as Fisher's exact test was used for the statistical analysis. When $p<0.05$, the difference between groups was considered to be statistically significant.

Results

Classification Test for Training the Deep Learning Model with Different Loss Functions

The effects of LR, MP, LA, SA, and LRS loss functions were compared on the classification performance of the Inception-v3 network model. The ROC curves of the Inception-v3 network model for X-ray image classification were presented in Figure 5 under different loss functions. It was found that the AUC of the original Inception-v3 network model was the smallest, while that after training with LRS loss function was the largest.

As could be discovered from Figure 6, the classification accuracy of the original model as well as the LR, MP, LA, SA, and LRS loss functions after training was 73.5%, 78.4%, 80.6%, 85.5%, 88.9%, and 90.7%, respectively. The AUC was 77.3%, 81.6%, 83.3%, 84.9%, 87.1%, and 89.6% respectively. The efficiency of the Inception-v3 network model trained under the LRS loss function was the best for X-ray image classification, so the LRS loss function was selected for the training of the Inception-v3 network model in this research.

X-Ray Image Segmentation under Faster-RCNN Model

The CNN, U-Net, Fast-RCNN, and Faster-RCNN models were compared in the effect of the identification of lesion regions in X-ray images, and the results are shown in Figure 7. All the models could recognize the lesion region in the X-ray image, but some models would identify the normal region as the lesion region. The identification performances of different models were quantitatively compared. It was found that the recall rate of the CNN, U-Net, Fast-RCNN, and Faster-RCNN models was 74.2%, 75.3%, 84.4%, and 89.7%, respectively for identifying the lesion region. The precision was 70.2%, 74.5%, 80.6%, and 87.3%, respectively; and the MAP was 0.614, 0.655, 0.754, and 0.802, respectively. Therefore, the Faster-RCNN model in this work showed the best efficiency for the identification of lesion regions in X-ray images.

Comparison of General Data of Patients with GCTB

The general data of included patients were compared between the PMMA group and the

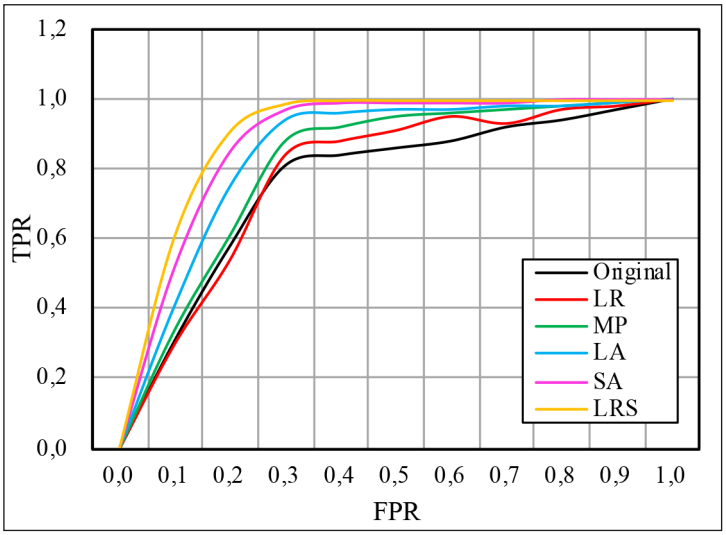

Figure 5. ROC curves of Inception-v3 network model under different loss functions.

RTP group, and the results are shown in Table I. There was no significant difference in the mean age, postoperative follow-up time, lesion location, and Campanacci grade between the PMMA group and the RTP group ($p>0.05$). The proportion of women in the RTP group was higher than that in the PMMA group obviously ($p<0.05$).

Prognosis of GCTB Patients with Different Treatment Methods

The local recurrence, MSTS score, and SF-36 score between the two groups were compared after follow-up, and the results are shown in Figure 8. The total recurrence of the two groups was 15.79% (3/19). There were 3 cases suffering from local recurrence in the PMMA group (1 case in the distal femur and 2 cases in the proximal tibia), and the recurrence was 25%. No one had a postoperative recurrence in the RTP group, and the difference in the postoperative local recurrence was not significant between the two groups ($p>0.05$). The MSTS score of the patients 3 months after the surgery was 27.08±0.90 of the PMMA group, and that of the RTP group was 24.14±1.22. The MSTS score of the PMMA group was higher than that of the RTP group, with a statistically significant difference ($p<0.05$). The postoperative SF-36 score of the PMMA group was 78.00±9.95, while that of the RTP group was 79.00±8.66. There was no significant difference in the long-term quality of life between the two groups ($p>0.05$).

The incidence of postoperative complications was also compared between the PMMA group and the RTP group, and the results are displayed in Figure 9. In the PMMA group, 1 case got a rejection reaction after surgery, and the symptoms

Table I. Comparison of general data of patients in PMMA and RTP groups.

General information	PMMA group	RTP group	*p*-value
Mean age (years old)	35.57±7.33	34.53±5.03	0.716
Gender, n (%)			
Female	8 (66.7%)	5 (71.4%)	
Male	4 (33.3%)	2 (28.6%)	0.000
Follow-up time (months)	13.67±4.54	12.43±4.65	0.577
Lesion location, n (%)			
Distal femur	5 (41.7%)	3 (42.9%)	
Proximal tibia	7 (58.3%)	4 (57.1%)	1.000
Campanacci grade, n (%)			
Grade I	2 (16.7%)	0	
Grade II	7 (58.3%)	4 (57.1%)	
Grade III	3 (25.0%)	3 (42.9%)	0.446

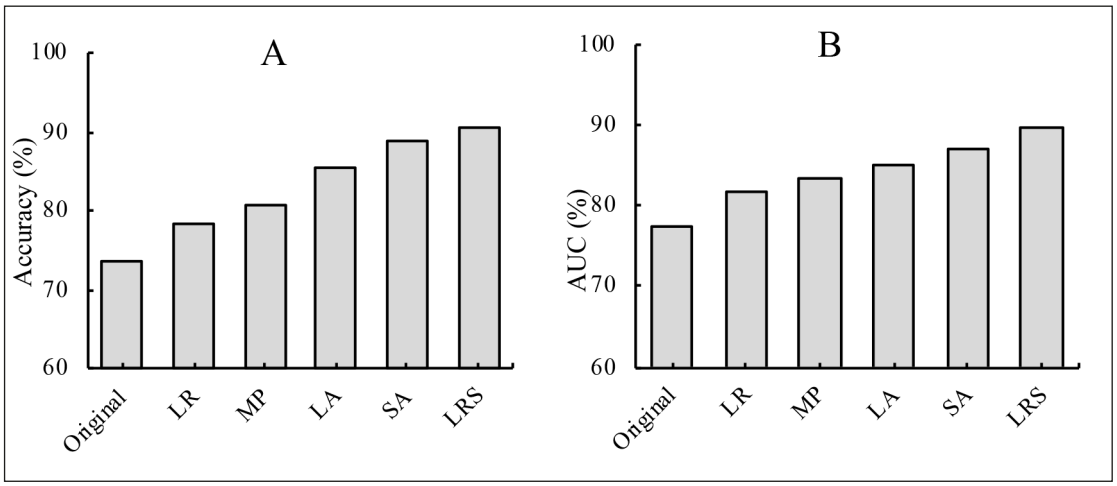

Figure 6. Comparison of the classification efficiency of the Inception-v3 network model under different loss functions. **A**, The classification accuracy. **B**, The AUC of the classification.

were relieved after the internal fixation was removed. 1 case had refracture, but the fracture healed after plaster immobilization. 2 cases had an infection of skin incision, and they were eventually recovered after standardized antibacterial treatment. In the RTP group, 1 case got deep vein thrombosis in the affected limb after surgery and then recovered well after thrombolysis. The rest of the patients in the RTP group did not have prosthesis loosening, dislocation, and other related

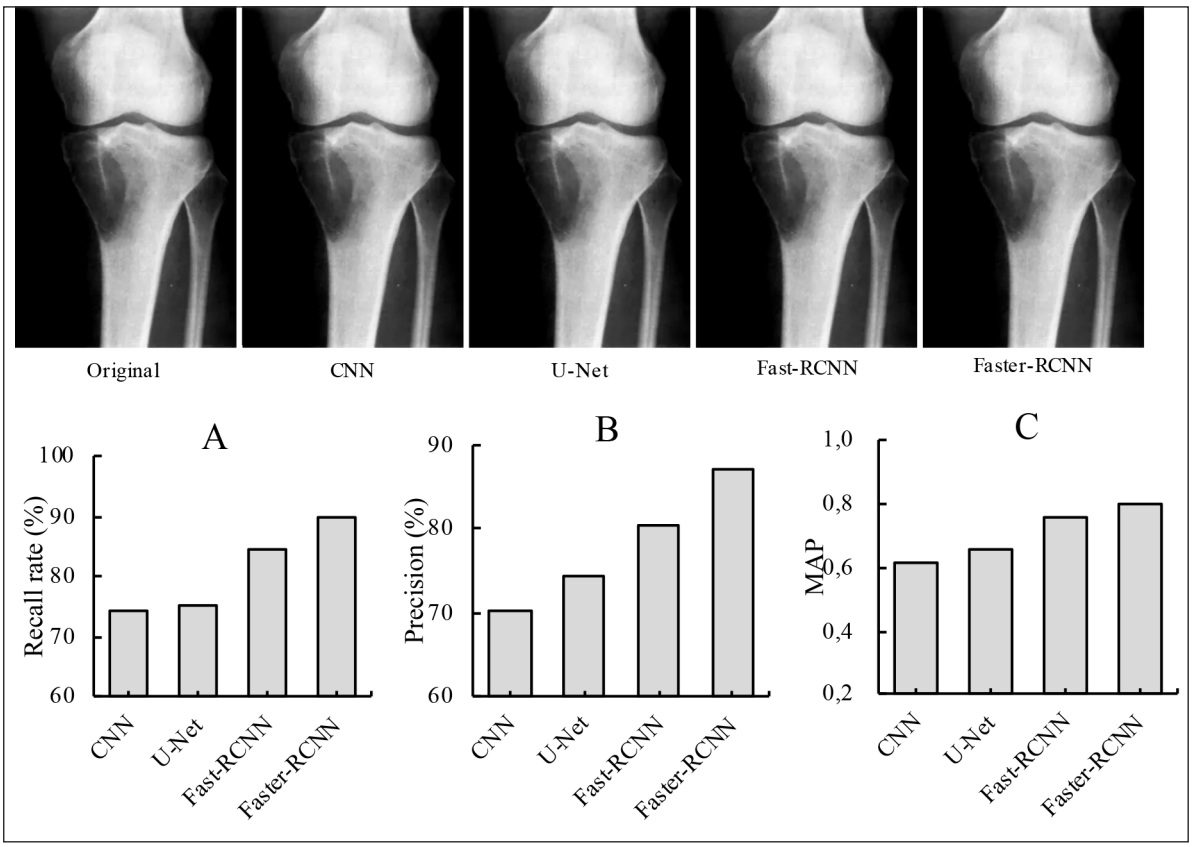

Figure 7. Comparison of identification effects of different deep learning models. **A**, Recall rate. **B**, Precision. **C**, MAP indicator.

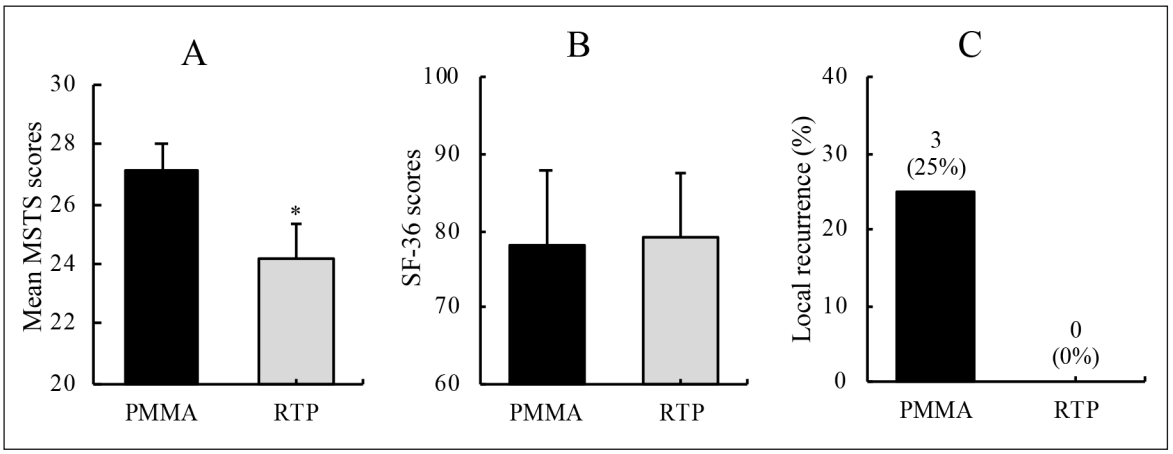

Figure 8. Comparison of postoperative recurrence, MSTS score, and quality of life of patients with GCTB. **A**, Mean MSTS score 3 months after surgery. **B**, Local recurrence after surgery. **C**, Postoperative SF-36 score. *indicated that the difference between groups was of statistical significance ($p<0.05$).

complications. However, no significant difference was found in the incidence of postoperative complications between the two groups after comparison ($p>0.05$).

X-Ray Image Evaluation of Postoperative Rehabilitation Effect in GCTB Patients

2 typical cases were selected out of the 19 patients for X-ray image evaluation of postoperative rehabilitation effect. The results are presented in Figure 10 and Figure 11. Typical case 1, a 33-year-old female patient, was diagnosed with recurrence 6 months after the surgery of the left proximal tibia. Then, she received denosumab for 3 months. The calcification around the lesion was found in the re-examination with clear boundaries, and the internal density of the lesion increased. After special RTP therapy and a 17-month follow-up, the patient had no tumor recurrence around the knee joint (Figure 10).

Typical case 2 was a 37-year-old female patient, and she was also diagnosed with recurrence 8 months after surgery of the right distal femur. After denosumab was given for 3 months, the re-examination revealed calcification of the lesion, and no obvious expansion of bone destruction was

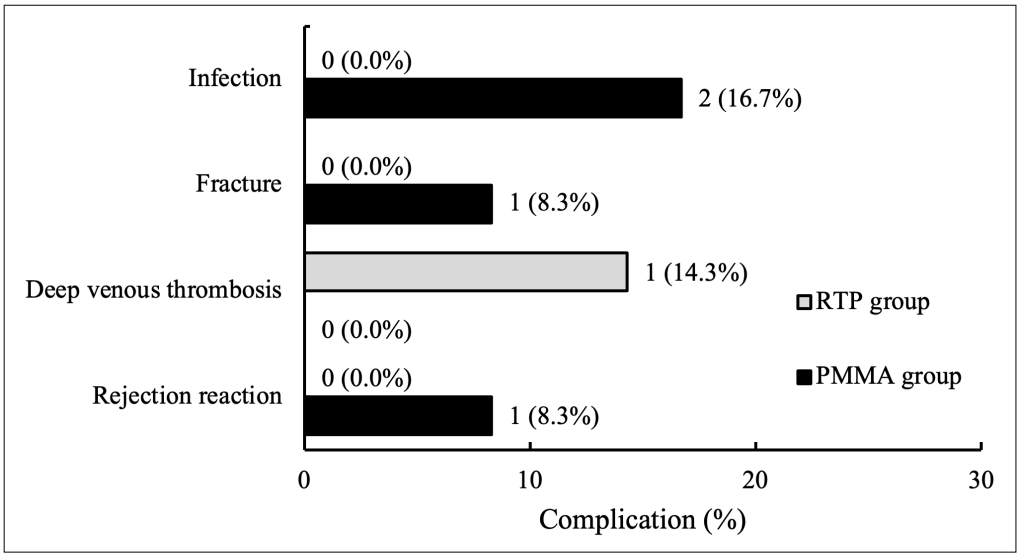

Figure 9. Comparison of postoperative complications in GCTB patients.

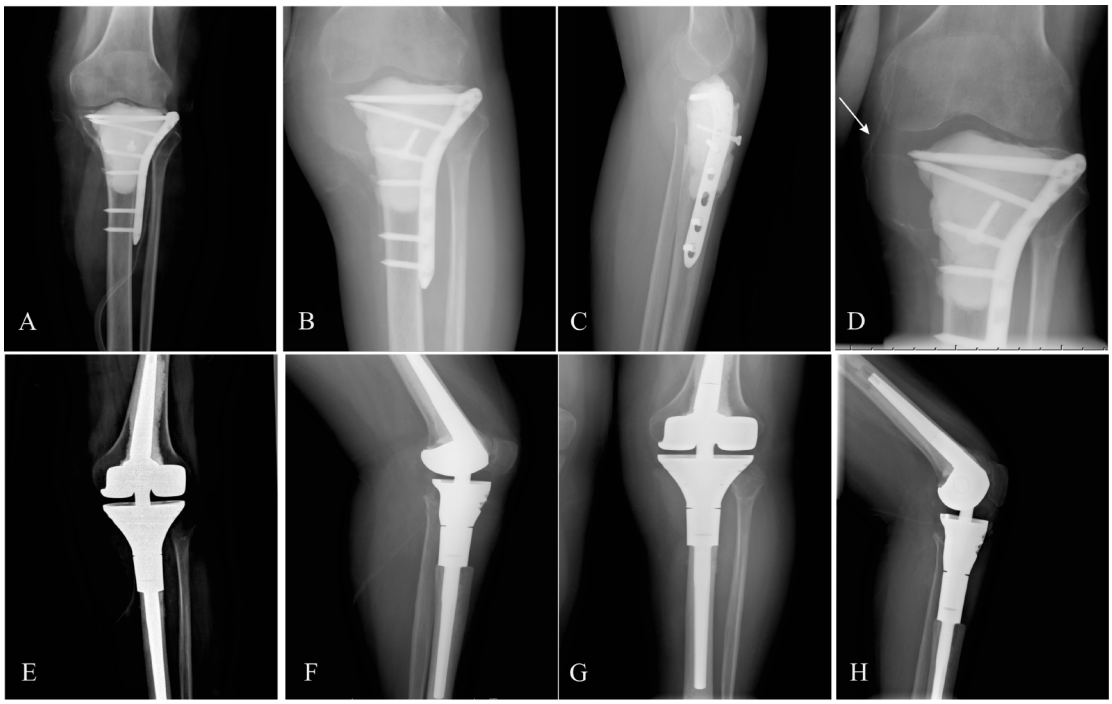

Figure 10. **A**, The X-ray image after the primary surgery. **B-C**, Tumor recurrence 6 months after the primary surgery. **D**, Perifocal calcification occurred 3 months after denosumab treatment. **E-F**, The X-ray images after the second surgery. **G-H**, No recurrence 17 months after joint replacement.

observed. The internal fixation device and bone cement retained by the previous surgery were removed, the field of view was further expanded, and the lesion spot was treated. PMMA internal fixation was performed again. With a 12-month follow-up postoperatively, it was found that no tumor recurred around the affected knee joint in this patient, as the process is displayed in Figure 11.

Discussion

Osteolytic destruction caused by GCTB is due to an imbalance between local osteogenesis and osteoclasts, and osteoclasts play an important role in this process[14]. GCTB is a more aggressive benign bone tumor that is not sensitive to radiotherapy and chemotherapy and is prone to recurrence after surgical treatment[15]. It has been confirmed that GCTB generally recurs 2 to 3 years after surgery, and the recurrence of the recurrent cases is 3.5 times that of the initial cases[16]. The denosumab adjuvant was beneficial in patients with recurrent and unresectable GCTB and was able to de-escalate the surgical plan in some patients with feasible surgical resection[17]. To this end, the effect was analyzed between the denosumab-assisted PMMA bone cement treatment and RTP therapy in the treatment of recurrent GCTB around the knee joint. The results suggested that there was no significant difference in the postoperative recurrence between the two groups after treatment, and the recurrence did not increase obviously. In the re-examination with imaging techniques such as X-ray, it was found that the tumor volume and the osteolytic range of GCTB patients decreased, while the density of the lesions gradually increased after the application of denosumab. There was also a conspicuous sclerosis zone around the tumor. These proved that denosumab could inhibit osteogenesis and eliminate the number of giant cells but cannot eliminate tumor stromal cells completely[18].

In this research, the Inception-v3 model was first used to classify the X-ray images of GCTB patients, and it was found that the Inception-v3 model had the best classification effect after training with the LRS loss function[19]. Secondly, the Faster-RCNN model was constructed to identify target regions in X-ray images of GCTB patients. The classification and identification effect of the Faster-RCNN model was remarkably better than that of CNN[20], U-Net[21] and Fast-RCNN[22] models. The results could provide a basis for the promotion and application of deep learning in medical

Figure 11. **A-B**, Tumor recurrence 6 months after the first surgery. **C-D**, Perifocal calcification occurred 3 months after denosumab treatment. **E-F**, X-ray images after the second surgery. **G-H**, No recurrence within 12 months after the second surgery.

science and could improve the clinical diagnosis of diseases. Some studies[23,24] have shown that PMMA bone cement can reduce the possibility of local recurrence after curettage in GCTB patients. This research proved that the probability of postoperative local recurrence in patients using PMMA was higher than that in RTP patients. This may be because a new sclerotic shell was formed around the lesion after denosumab application, and tumor cells were distributed in the sclerotic bone, which increased the difficulty of curettage surgery[25,26]. Denosumab can cause soft tissue fibrosis and adhesions around the tumor and also increases the difficulty of intracapsular curettage[27]. Subsequently, the MSTS scores of patients after different surgical treatments were compared in this work, and that of patients in the PMMA group was significantly higher than that in the RTP group. This was perhaps due to the simultaneous removal of normal bone and soft tissues (like muscles and ligaments) around the patient's knee joint when treated with extensive-resection RTP[28,29]. Some studies[30] have also confirmed that PMMA would cause thermal damage, and the surgical method of scraping PMMA bone cement filling could damage the subarticular cartilage, leading to the incidence of long-term osteoarthritis. In this research, only 1 patient with PMMA had a postoperative infection, so there was no statistical significance compared with the RTP group.

Conclusions

Denosumab was an effective adjuvant therapy for recurrent GCTB around the knee joint, but extensive-resection RTP was recommended to reduce the risk of local recurrence after denosumab treatment. Although the lower limb function of patients after this treatment method was not as good as that of the PMMA bone cement treatment, it met the needs of the patients' basic daily activities. However, the number of samples included was few, and all surgeries were performed by the same group of physicians, so the findings could not be replicated. For the different shapes and sizes of individual tumors and their adjacent relationship with important nerves and blood vessels, multi-center large-sample research is needed to explore further and verify the effectiveness of this method. In conclusion, the results of this research could offer a reference for the selection of treatment methods for patients with recurrent GCTB around the knee joint.

Conflict of Interest
The Authors declare that they have no conflict of interests.

Funding
This work was supported by the Medical Science Research Plan in Hebei Province (Project No. 20220492) and the Science and Technology Research and Development Plan Project of Handan (Project No. 21422083062).

Ethics Approval
This study was approved by the Ethics Committee of The First Hospital of Handan (Approval number: 2023-L-005).

Informed Consent
All patients included signed the informed consent.

Authors' Contributions
All authors of this paper have made substantial (or major) contributions to the whole process of study design, data collection, data analysis and paper writing.

Data Availability
The data generated by this study is publicly available, and the authors may provide relevant data upon request.

ORCID ID
Guo-Chuan Zhang: 0000-0002-2837-5352.

References

1) Montgomery C, Couch C, Emory CL, Nicholas R. Giant Cell Tumor of Bone: Review of Current Literature, Evaluation, and Treatment Options. J Knee Surg 2019; 32: 331-336.
2) Şirin E, Akgülle AH, Topkar OM, Sofulu Ö, Baykan SE, Erol B. Mid-term results of intralesional extended curettage, cauterization, and polymethylmethacrylate cementation in the treatment of giant cell tumor of bone: A retrospective case series. Acta Orthop Traumatol Turc 2020; 54: 524-529.
3) Kito M, Matsumoto S, Ae K, Tanizawa T, Gokita T, Hayakawa K, Funauchi Y, Yamamoto N. Giant cell tumor of the distal femur: Outcome beyond 20 years of follow-up after curettage with polymethylmethacrylate. J Orthop Sci 2018; 23: 1051-1055.
4) van der Heijden L, Dijkstra PDS, Blay JY, Gelderblom H. Giant cell tumour of bone in the denosumab era. Eur J Cancer 2017; 77: 75-83.
5) Hayashida K, Kawabata Y, Kato I, Kamiishi T, Matsuo K, Takeyama M, Inaba Y. Clinical and pathological analysis of giant cell tumor of bone with denosumab treatment and local recurrence. J Orthop Sci 2022; 27: 215-221.
6) Xu L, Jin J, Hu A, Xiong J, Wang D, Sun Q, Wang S. Soft tissue recurrence of giant cell tumor of the bone: Prevalence and radiographic features. J Bone Oncol 2017; 9: 10-14.
7) Li H, Gao J, Gao Y, Lin N, Zheng M, Ye Z. Denosumab in Giant Cell Tumor of Bone: Current Status and Pitfalls. Front Oncol 2020; 10: 580605.
8) Lipplaa A, Dijkstra S, Gelderblom H. Challenges of denosumab in giant cell tumor of bone, and other giant cell-rich tumors of bone. Curr Opin Oncol 2019; 31: 329-335.
9) Tsukamoto S, Mavrogenis AF, Tanzi P, Leone G, Ciani G, Righi A, Akahane M, Honoki K, Tanaka Y, Donati DM, Errani C. Denosumab for Bone Giant Cell Tumor of the Distal Radius. Orthopedics. 2020; 43: 284-291.
10) Oguro S, Okuda S, Sugiura H, Matsumoto S, Sasaki A, Susa M, Morioka H, Jinzaki M. Giant Cell Tumors of the Bone: Changes in Image Features after Denosumab Administration. Magn Reson Med Sci 2018; 17: 325-330.
11) Çallı E, Sogancioglu E, van Ginneken B, van Leeuwen KG, Murphy K. Deep learning for chest X-ray analysis: A survey. Med Image Anal 2021; 72: 102125.
12) Esfandiari H, Weidert S, Kövesházi I, Anglin C, Street J, Hodgson AJ. Deep learning-based X-ray inpainting for improving spinal 2D-3D registration. Int J Med Robot 2021; 17: e2228.
13) Niehues SM, Adams LC, Gaudin RA, Erxleben C, Keller S, Makowski MR, Vahldiek JL, Bressem KK. Deep-Learning-Based Diagnosis of Bedside Chest X-ray in Intensive Care and Emergency Medicine. Invest Radiol 2021; 56: 525-534.
14) Noh BJ, Park YK. Giant cell tumor of bone: updated molecular pathogenesis and tumor biology. Hum Pathol 2018; 81: 1-8.
15) Ventura L, Petrella E, Piciucchi S, Cilli E, Luiselli D, Feeney RNM, Traversari M. Giant cell tumor of bone in an eighteenth-century Italian mummy. Virchows Arch 2021; 479: 1255-1261.
16) Araki Y, Yamamoto N, Hayashi K, Takeuchi A, Miwa S, Igarashi K, Taniguchi Y, Yonezawa H, Morinaga S, Tsuchiya H. Secondary Osteoarthritis After Curettage and Calcium Phosphate Cementing for Giant-Cell Tumor of Bone Around the Knee Joint: Long-Term Follow-up. JB JS Open Access 2020; 5: e19.00068.
17) Perrin DL, Visgauss JD, Wilson DA, Griffin AM, Abdul Razak AR, Ferguson PC, Wunder JS. The role of Denosumab in joint preservation for patients with giant cell tumour of bone. Bone Joint J 2021; 103-B: 184-191.
18) Stadler N, Fingernagel T, Hofstaetter SG, Trieb K. A recurrent giant cell tumor of bone treated with denosumab. Clin Pract 2015; 5: 697.
19) Govinahallisathyanarayana S, Acton ST, Hossack JA. Closed-Loop Low-Rank Echocardiographic Artifact Removal. IEEE Trans Ultrason Ferroelectr Freq Control 2021; 68: 510-525.

20) Mate GS, Kureshi AK, Singh BK. An Efficient CNN for Hand X-Ray Classification of Rheumatoid Arthritis. J Healthc Eng 2021; 2021: 6712785. Erratum in: J Healthc Eng 2021; 2021: 9808309.

21) Nishitani Y, Nakayama R, Hayashi D, Hizukuri A, Murata K. Segmentation of teeth in panoramic dental X-ray images using U-Net with a loss function weighted on the tooth edge. Radiol Phys Technol 2021; 14: 64-69.

22) Liu B, Luo J, Huang H. Toward automatic quantification of knee osteoarthritis severity using improved Faster R-CNN. Int J Comput Assist Radiol Surg 2020; 15: 457-466.

23) Benevenia J, Rivero SM, Moore J, Ippolito JA, Siegerman DA, Beebe KS, Patterson FR. Supplemental Bone Grafting in Giant Cell Tumor of the Extremity Reduces Nononcologic Complications. Clin Orthop Relat Res 2017; 475: 776-783.

24) Chen EA, Caruana DL, Khan FA. Management of an Unusual Periprosthetic Giant Cell Tumor of Bone of the Proximal Tibia. J Am Acad Orthop Surg Glob Res Rev 2018; 2: e012.

25) Greenberg DD, Lee FY. Bisphosphonate-loaded Bone Cement as a Local Adjuvant Therapy for Giant Cell Tumor of Bone: A 1 to 12-Year Follow-up Study. Am J Clin Oncol 2019; 42: 231-237.

26) Lipplaa A, Dijkstra S, Gelderblom H. Challenges of denosumab in giant cell tumor of bone, and other giant cell-rich tumors of bone. Curr Opin Oncol 2019; 31: 329-335.

27) Latorre MR, Albergo JI, Farfalli GL, Roitman PD, Plantalech L, Ayerza MA, Aponte-Tinao LA. Denosumab como tratamiento neoadyuvante del tumor de células gigantes del hueso. Indicaciones, resultados y efectos adversos [Denosumab as a treatment for giant cell tumor of bone. Indications, results and side effects]. Medicina (B Aires) 2021; 81: 767-773.

28) Yilmaz M, Sørensen MS, Saebye C, Baad-Hansen T, Petersen MM. Long-term results of the Global Modular Replacement System tumor prosthesis for reconstruction after limb-sparing bone resections in orthopedic oncologic conditions: Results from a national cohort. J Surg Oncol 2019; 120: 183-192.

29) Arifeen KN, Mahmud CI, Chowdhury AZ, Selimullah AM, Faisal MA, Kundu IK, Ali MH. Early Functional Outcome of Wide Resection and Endoprosthesis Replacement for Recurrent Giant Cell Tumour of the Distal Femur. Mymensingh Med J 2020; 29: 202-208.

30) Spindel J, Chrobok A, Mrozek T, Tomasik P, Matysiakiewicz J. Evaluation of methods of bone defect reconstruction after iliac tumor resections. Ortop Traumatol Rehabil 2005; 7: 590-594.